ORIGINAL PAPER

A competitive-type photoelectrochemical aptasensor for 17 beta-estradiol detection in microfluidic devices based on a novel Au@Cd:SnO$_2$/SnS$_2$ nanocomposite

Yonglun Zhang[1] · Shihua Zhang[1] · Zijing Xu[1] · Jiaxing Zhang[1] · Zhuangzhuang Qu[1] · Weilu Liu[1]

Abstract

A competitive-type photoelectrochemical (PEC) aptasensor coupled with a novel Au@Cd:SnO$_2$/SnS$_2$ nanocomposite was designed for the detection of 17β-estradiol (E2) in microfluidic devices. The designed Au@Cd:SnO$_2$/SnS$_2$ nanocomposites exhibit high photoelectrochemical activity owing to the good matching of cascade band-edge and the efficient separation of photo-generated e$^-$/h$^+$ pairs derived from the Cd-doped defects in the energy level. The Au@Cd:SnO$_2$/SnS$_2$ nano-composites were loaded into carbon paste electrodes (CPEs) to immobilize complementary DNA (cDNA) and estradiol aptamer probe DNA (E2-Apt), forming a double-strand DNA structure on the CPE surface. As the target E2 interacts with the double-strand DNA, E2-Apt is sensitively released from the CPE, subsequently increasing the photocurrent intensity due to the reduced steric hindrance of the electrode surface. The competitive-type sensing mechanism, combined with high PEC activity of the Au@Cd:SnO$_2$/SnS$_2$ nanocomposites, contributed to the rapid and sensitive detection of E2 in a "signal on" manner. Under the optimized conditions, the PEC aptasensor exhibited a linear range from 1.0×10^{-13} mol L^{-1} to 3.2×10^{-6} mol L^{-1} and a detection limit of 1.2×10^{-14} mol L^{-1} (S/N = 3). Moreover, the integration of microfluidic device with smartphone controlled portable electrochemical workstation enables the on-site detection of E2. The small sample volume (10 μL) and short analysis time (40 min) demonstrated the great potential of this strategy for E2 detection in rat serum and river water. With these advantages, the PEC aptasensor can be utilized for point-of-care testing (POCT) in both clinical and environmental applications.

Keywords Photoelectrochemical sensor · Modified electrode · Au@Cd:SnO$_2$/SnS$_2$ nanocomposites · Label-free · Competitive-type · 17β-Estradiol · Microfluidic devices

Introduction

17β-Estradiol (E2), a widely distributed estrogen in the bodies of humans and animals, plays a significant role in biological growth, reproduction, and development [1, 2]. Additionally, E2 is utilized as a pharmaceutical for contraception, hormone therapy, and animal husbandry [3]. The abuse of E2 leads to the accumulation of its residues in the environment, which can pose health risks to humans through the enrichment of the food chain. This could increase the risk of infertility, breast cancer, and ovarian cancer [4, 5].

Traditional methods for the measurement of E2 levels typically rely on high performance liquid chromatography-mass (HPLC/MS) and gas chromatography-mass (GC/MS) [6, 7]. These methods are generally costly, time-consuming, and reliant on laboratory facilities. Therefore, to meet the need for E2 detection in actual samples, the development of affordable, highly stable, sensitive, and user-friendly point-of-care testing (POCT) devices for quantitative detection holds significant implications for both biological analysis and environmental monitoring. One promising approach in developing POCT devices is combining microfabricated devices with portable optical and electrochemical sensors [8–10].

Photoelectrochemical (PEC) sensors have attracted attention because of their low background signals, high sensitivity, simple operation, and miniaturization capabilities [11]. However, most PEC sensors often use drop-coating to load

✉ Weilu Liu
  liuweilulucky@163.com

1 School of Pharmacy, Shenyang Pharmaceutical University, Shenyang 110016, PR China

material onto the electrode surface. This approach limits the amount of material that can be loaded and the strength of the bond. The loosely bound materials tend to fall off during subsequent sensor modification and testing, affecting the sensor's stability [12]. To solve the above problems, we innovatively used carbon paste electrodes (CPEs) as the working electrode of the PEC sensor. The CPEs were prepared by a simple grinding and filling process to achieve a uniform loading of the material, and the electrodes can be reused by grinding, which has good stability and repeatability [13–15]. The CPEs can accommodate a greater quantity of materials, which provides enough binding sites for the recognition unit, leading to a PEC sensor with high sensitivity and good selectivity.

The sensitivity of a PEC sensor relies on the properties of the photoactive materials [16]. Recently, tin-based nanocomposites have garnered attention due to their favorable biocompatibility, low toxicity, and cost-effectiveness [17, 18]. However, single tin-based materials often have various disadvantages that limit their application in PEC sensors. For instance, SnO_2 cannot generate photocurrents in the visible light range due to its wide band gap (3.5–3.6 eV) [19]. SnS_2 has a suitable band gap (2.2–2.3 eV) and light absorption capabilities, but its photocurrent response is hindered by rapid electron-hole recombination [20]. The formation of a type-II heterojunction by SnO_2 and SnS_2 can enhance the separation efficiency of electrons and holes (e^-/h^+), expanding light absorption and resulting in a heightened photocurrent response [21]. Nevertheless, the photoelectric activity of SnO_2/SnS_2 still requires further enhancement for the sensitive detection of low concentration analytes in complex samples.

The recognition element is of great importance for the PEC sensing system to acquire exceptional selectivity. Aptamers are short single-stranded RNA or DNA oligonucleotides that can capture specific targets and fold into a rigid three-dimensional (3D) double helix structure through complementary base-pairing [22, 23]. Aptamer synthesis and screening usually involve the in vitro selection process known as systematic evolution of ligands by exponential enrichment (SELEX) [24]. Several aptamer sequences of E2 have been reported [25, 26], and the most commonly used aptamer with a 76-mer sequence has been validated to exhibit high E2-specific binding capacity with K_D value of 11 nmol [27]. This 76-mer E2 aptamer (E2-Apt) can serves as a promising recognition element for selective detection of E2 in complex samples.

In this work, we developed a PEC aptasensor for the sensitive detection of E2 based on a competitive-type aptamer structure. A novel type-II Au@Cd:SnO_2/SnS_2 heterojunction with high photoelectric activity was designed as the electrode material doped in the CPE. Elemental doping is a widely used simple and effective strategy for modulating semiconductor properties [28, 29]. By doping of Cd elements into SnO_2/SnS_2 heterojunction, defective electronic off-domains can introduce between the conduction and valence bands of the semiconductor, so that the photogenerated electrons can jump to the trap energy levels and reduce the compounding rate of photogenerated electrons and holes, which improves the response of PEC [30]. Meanwhile, the loading of gold nanoparticles onto Cd:SnO_2/SnS_2 further extends the visible light absorption range.

Furthermore, a competitive-type double-stranded structure was designed as the recognition unit. As shown in Scheme 1, a sulfhydryl-modified complementary short-stranded DNA (cDNA) was anchored on Au@Cd:SnO_2/SnS_2-modified CPE via Au-S bonding. The E2-Apt is further immobilized via hybridization with the pre-anchor cDNA, forming double-stranded structure. When target E2 is incubated on the electrode, the E2-Apt would be released from the electrode surface to capture with E2, resulting in the photocurrent increase due to the reduction of steric hindrance on the CPE. The increase in photocurrent was found to be linearly dependent on E2 concentrations, resulting in a "signal on" sensing manner. Under the optimized conditions, the PEC aptasensor exhibits a wide linear range, a femtomole level detection limit and a good selectivity for E2 detection. Moreover, the designed microfluidic device contributed to the convenient detection of E2 in serum and river water samples in a POCT manner.

Experimental

The details of materials, reagents, and apparatus were shown in the Supporting Information.

Synthesis of Au@Cd:SnO_2/SnS_2 nanocomposites

The Cd:SnO_2/SnS_2 was prepared using a modified procedure previously reported [31]. Typically, 5.0 mmol of $SnCl_4\cdot5H_2O$ and 0.5 mmol of $CdCl_2\cdot5H_2O$ were dissolved in 30 mL of ultrapure water. The uniform suspension was obtained after adding 8.0 mmol of thioacetamide (TAA) and stirring for 30 min. The suspension was transferred to a Teflon-sealed autoclave and reacted at 190 ℃ for 12 h. The mixture was centrifuged and washed several times with deionized water and anhydrous ethanol, and the product was obtained by vacuum drying at 60 °C overnight.

Au@Cd:SnO_2/SnS_2 was prepared by a typical method. 0.50 g of Cd:SnO_2/SnS_2 was added to 100 mL of distilled water and sonicated for 30 min. Under vigorous stirring, 2.4 mL of $HAuCl_4\cdot4H_2O$ was added dropwise to the mixed suspension, and then heated to 80 ℃ and stirred for 10 min. Next, 6 mL of 0.034 mol L^{-1} sodium citrate solution was rapidly added, and stirring was continued at 80 ℃ for

Scheme 1 The schematic of competitive-type PEC microfluidic aptasensor
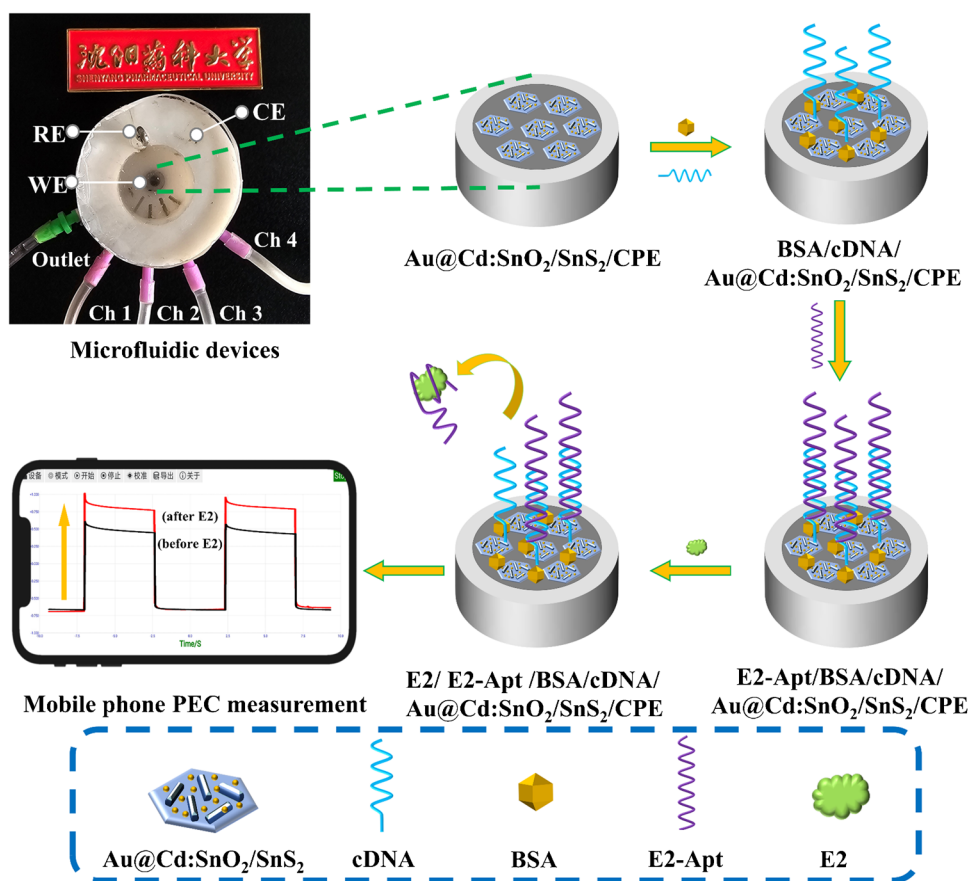
30 min. The obtained gray-yellow product was collected by centrifugation and washing, followed by drying at 60 ℃ in vacuum for 12 h.

Fabrication and detection of label-free competitive-type PEC aptasensor

The CPE containing mixed photoelectric materials (Au@Cd:SnO$_2$/SnS$_2$/CPE) was prepared by mixing graphite powder, liquid paraffin, and different ratios of Au@Cd:SnO$_2$/SnS$_2$ powder. The mixture was ground in an agate mortar for 30 min to achieve homogeneity and dried in a 30 ℃ oven for 6 h to reach its optimal state. Subsequently, the mixture was tightly filled into a Teflon hollow tube (i.d. 2.0 mm) with a filling height of 3 mm, while a copper wire was used as the electrical contact. Before each use, the electrode surface was polished with sulfate paper and cleaned with water. The prepared CPE was shown in Fig. S1.

The process of constructing a competitive-type PEC aptasensor was shown in Scheme 1. First, 7 μL of cDNA (0.1 μmol L^{-1}) and 1 μL of TCEP (10 mmol L^{-1}) were mixed and heated in a water bath at 90 ℃ for 5 min, and then slowly cooled to room temperature. The mixture was then dropped on the previously prepared Au@Cd:SnO$_2$/SnS$_2$/CPE (from channel 1), incubated overnight at 4 ℃ to immobilize the

cDNA on the electrode via Au-S bonding, and washed with 10 mmol L^{-1} PBS (pH 7.4) to remove unbound cDNA. To prevent non-specific binding, 7 μL bovine serum albumin (BSA 1 wt%) was dropped on the electrode (from channel 2), incubated for 30 min, and then rinsed with PBS.

Finally, 7 μL of E2-Apt (0.2 μmol L^{-1}) solution was dropped on the electrode surface (from channel 3) and incubated at 4 ℃ for 1 h. The electrode was then washed with PBS to construct E2-Apt/BSA/cDNA/Au@Cd:SnO$_2$/SnS$_2$/CPE. Then, 10 μL of various concentrations of E2 solution was incubated on the E2-Apt/BSA/cDNA/Au@Cd:SnO$_2$/SnS$_2$/CPE for 40 min at 37 ℃ (from channel 4), followed by thorough washing with PBS before performing the photocurrent measurement.

Regeneration of PEC aptasensor

To regenerate the sensor, the copper wire at the top of the CPE was pushed out until the carbon paste mixture was exposed for about 0.2 mm and then polished on sulfate paper to obtain a new electrode interface. Subsequently, the new sensor was completed by connecting the aptamer as described in the "Fabrication and detection of label-free competitive-type PEC aptasensor" section.

Photoelectric chemical detection

The photoelectrochemical measurement was conducted by a three-electrode system with a CPE as the working electrode, Ag/AgCl as the reference electrode, and a platinum wire electrode as the counter electrode. The changes in the photocurrent response of 0.1 mol L^{-1} AA (0.1 mol L^{-1} PBS, pH 7.4) on E2-Apt/BSA/cDNA/ Au@Cd:SnO$_2$/SnS$_2$/CPE were recorded to complete the measurement. The excitation light source was a 200 W LED white light, which was switched every 20 s, and the applied voltage was 0 V.

Results and discussions

Characterization of cd:SnO$_2$/SnS$_2$ and Au@Cd:SnO$_2$/SnS$_2$

The morphology and microstructure of the Cd:SnO$_2$/SnS$_2$ and Au@Cd:SnO$_2$/SnS$_2$ nanocomposites were characterized.

Figure 1A–D shows the transmission electron microscopy (TEM) images of SnO$_2$, SnS$_2$, Cd:SnO$_2$/SnS$_2$, and Au@Cd:SnO$_2$/SnS$_2$, respectively. As shown in Fig. 1A, the SnO$_2$ is a particle structure with 5–10 nm diameters. Figure 1B shows that SnS$_2$ is a multi-layer hexagonal flake structure with sizes 60–80 nm diameters. As shown in Fig. 1C and D, there is no significant difference in structure and morphology between Cd:SnO$_2$/SnS$_2$ and Au@Cd:SnO$_2$/SnS$_2$, comprised of multi-layer hexagonal flakes of SnS$_2$ (~100 nm) with rod-like SnO$_2$ (~20 nm) dispersed on the surface. The SnS$_2$ flakes and SnO$_2$ rods in the nanocomposites are larger and more dispersed compared to Fig. 1A and B. The material of 1 mg mL^{-1} dispersed water solution color changes from orange-yellow (inset of Fig. 1C) to gray-yellow (inset of Fig. 1D), which could suggest that the Au@Cd:SnO$_2$/SnS$_2$ was successfully prepared. Figure 1E shows the scanning electron microscopy (SEM) images of Cd:SnO$_2$/SnS$_2$, a block-like particle composed of multi-layer flakes. After loading a large amount of Au nanoparticles, the Au@Cd:SnO$_2$/SnS$_2$ in Fig. 1F became rougher, facilitating the
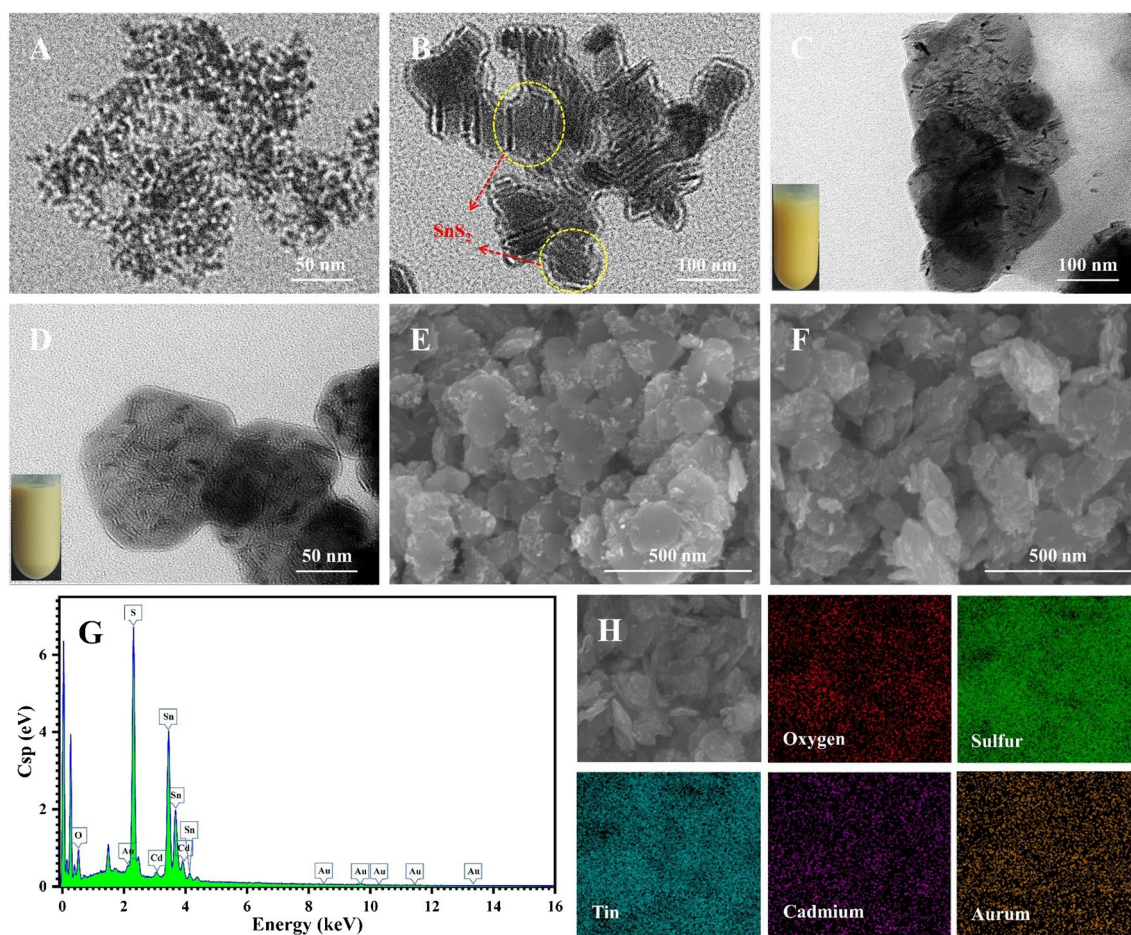

Fig. 1 TEM images of **A** SnO$_2$, **B** SnS$_2$, **C** Cd:SnO$_2$/SnS$_2$, and **D** Au@Cd:SnO$_2$/SnS$_2$, SEM images of **E** Cd:SnO$_2$/SnS$_2$, **F** Au@Cd:SnO$_2$/SnS$_2$; **G** EDS spectrum of Au@Cd:SnO$_2$/SnS$_2$; **H** SEM mapping region of Au@Cd:SnO$_2$/SnS$_2$ and element mapping images

immobilization and binding of more cDNA. Figure 1G and H show the energy dispersive spectrometer (EDS) point scan results and mapping images of Au@Cd:SnO$_2$/SnS$_2$. These figures clearly show that the nanocomposites contain O, S, Sn, Cd, and Au elements, demonstrating the successful preparation of Au@Cd:SnO$_2$/SnS$_2$.

Figure 2A shows the X-ray power diffraction (XRD) patterns of the synthesized Cd:SnO$_2$/SnS$_2$ (curve-a) and Au@Cd:SnO$_2$/SnS$_2$ (curve-b) materials. Multiple significant characteristic peaks appearing at 15.03°, 28.20°, 32.12°, 49.96°, and 52.45° are attributed to the (001), (100), (101), (110), and (111) crystal planes of the tetragonal phase SnS$_2$ (JCPDS No.23–0677) [20], while the characteristic peaks appearing at 26.61°, 33.89°, 37.95°, 51.78°, and 65.94° can be attributed to the (110), (101), (200), (211), and (301) crystal planes of the hexagonal phase SnO$_2$ (JCPDS No.41-1445) [19]. Both indicate that the SnO$_2$/SnS$_2$ composites were successfully synthesized and the absence of characteristic peaks of Cd in the spectrum may be due to the low doping amount. In addition, by comparing curves a and b, weak peaks are clearly observed at 38.27°, 44.60°, 64.68°, and 77.55° on curve-b, which correspond to the (111), (200), (220), and (311) crystal planes of the characteristic diffraction peaks of Au (JCPDS No.01-1172) [32]. It is indicated that Au was successfully loaded on the surface of Cd:SnO$_2$/SnS$_2$.

Figure 2B shows the UV–vis absorption spectra of SnO$_2$, SnS$_2$, Cd:SnO$_2$/SnS$_2$, and Au@Cd:SnO$_2$/SnS$_2$. The SnO$_2$ (curve-a) and SnS$_2$ (curve-b) exhibit weak absorption in the spectrum below 400 nm in the UV. The significant energy bandgap (~3.67 eV) limits the efficient utilization of light, leading to reduced separation between photo-generated electron-hole pairs (e$^-$/h$^+$) and consequently decreasing the efficiency of photocurrent conversion. Trap energy levels are introduced by doping Cd ions in SnO$_2$/SnS$_2$ to promote visible light absorption. As a result, the absorption wavelength of Cd:SnO$_2$/SnS$_2$ (curve-c) extends up to 600 nm, and the absorption intensity is also enhanced. Furthermore, when Au is loaded, it also absorbs visible light, which

further increases the optical absorption intensity of the Au@Cd:SnO$_2$/SnS$_2$ (curve-d).

In addition, elemental analysis of Au@Cd:SnO$_2$/SnS$_2$ was performed using X-ray photoelectron spectroscopy (XPS). Figure 3A shows the full spectrum and a series of high-resolution XPS spectra of Cd 3d, O 1s, Sn 3d, S 2p, and Au 4 f. Figure 3B shows the Cd 3d spectrum, in which the two peaks at 412.2 eV and 405.4 eV correspond to Cd^{3+} 3d$_{3/2}$ and Cd^{3+} 3d$_{5/2}$, respectively [33]. Figure 3C shows the O^{2-} 1s spectrum, in which the peak at 531.5 eV binding energy is attributed to the Sn-O bond. Figure 3D shows two peaks at 494.6 eV and 486.2 eV, which correspond to Sn^{4+} 3d$_{3/2}$ and Sn^{4+} 3d$_{5/2}$ in SnO$_2$/SnS$_2$. In Fig. 3E, the binding energies of 167.7 eV and 166.5 eV correspond to S^{2-} 2p$_{1/2}$ and S^{2-} 2p$_{3/2}$, respectively. The shift to the low-energy region could be attributed to the binding of Au-S causing the shift of S element binding energy. In Fig. 3F, the binding energies of zero-valent Au 4f$_{7/2}$ and Au 4f$_{5/2}$ are respectively responsible for the two peaks observed at 87.5 eV and 83.9 eV. The above XPS analysis results further confirm the successful preparation of Au@Cd:SnO$_2$/SnS$_2$.

PEC performance of materials

To obtain the highest photocurrent response value, the effect of the proportion of different components of Au@Cd:SnO$_2$/SnS$_2$ nanocomposites on the photocurrent response was investigated. By modulating the proportions of Sn source, S source, and Cd doping during synthesis, we have successfully identified the material Au@Cd:SnS$_2$/SnO$_2$-(d) (Table S1). It exhibits a higher photovoltaic response value, which can be used as an optimal substrate for subsequent sensor construction.

Simultaneously, the PEC response of different CPEs made from various materials was investigated under visible light irradiation. Figure 4A shows that the bare CPE represented by curve-a has the lowest light-induced current response. SnO$_2$ (curve-b) and SnS$_2$ (curve-c) show weak photoelectric current responses, while the photoelectric current of the

Fig. 2 A XRD patterns of (a) Cd:SnO$_2$/SnS$_2$ and (b) Au@Cd:SnO$_2$/SnS$_2$; **B** UV-vis absorption spectra of (a) SnO$_2$, (b) SnS$_2$, (c) Cd:SnO$_2$/SnS$_2$, and (d) Au@Cd:SnO$_2$/SnS$_2$
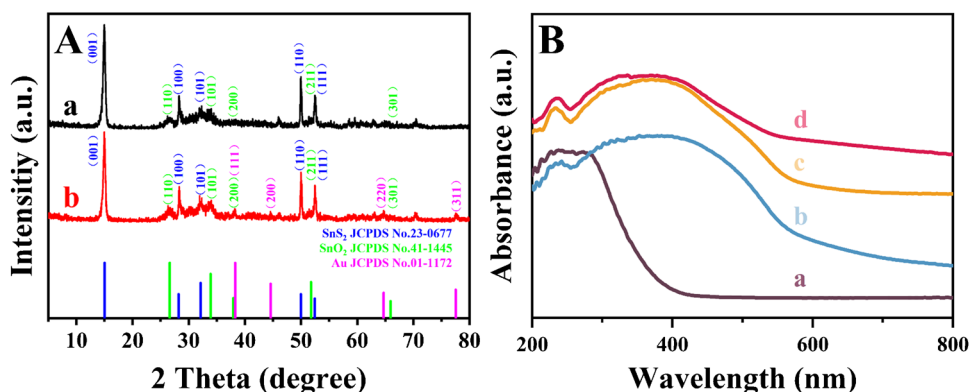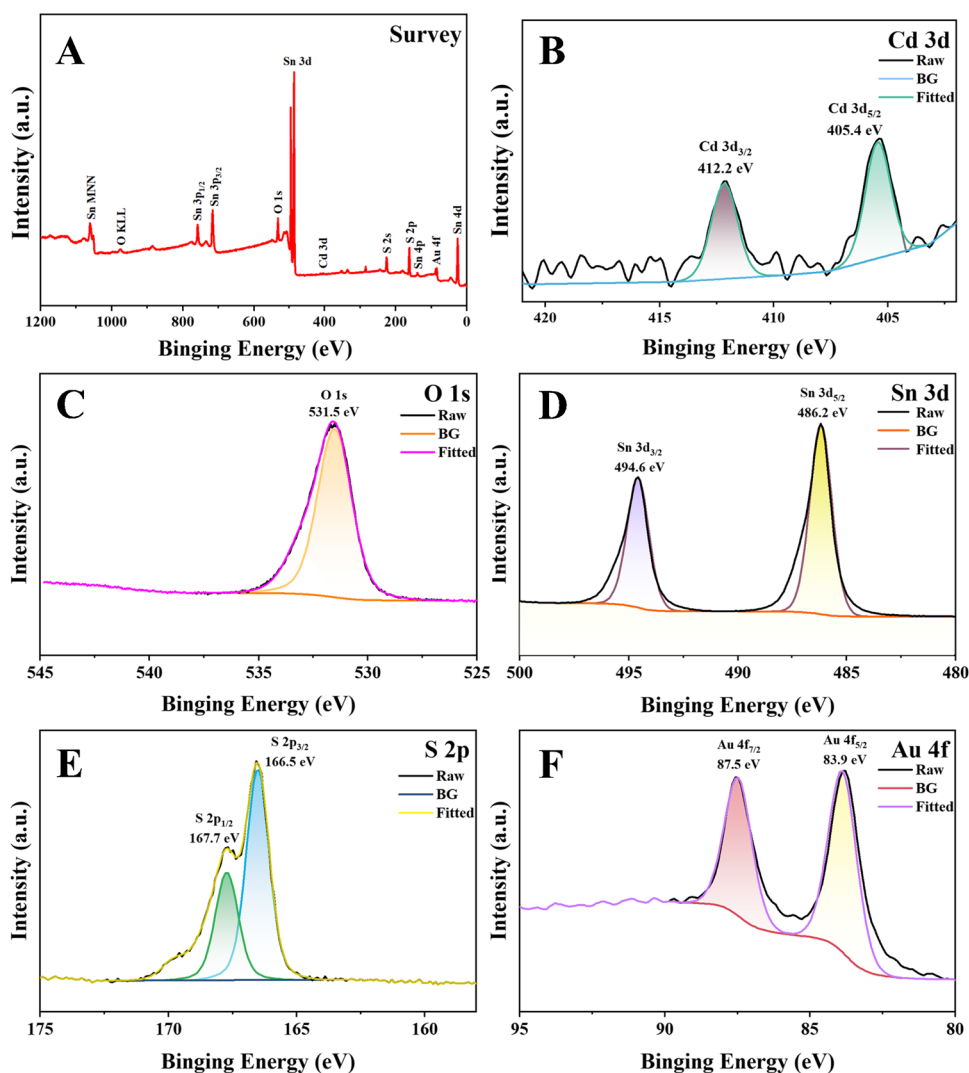
Fig. 3 XPS spectra of Au@
Cd:SnO$_2$/SnS$_2$ nanocomposites:
A full-scans, high-resolution
spectrum of (**B**) Cd, (**C**) O,
(**D**) Sn, (**E**) S, (**F**) Au

SnO$_2$/SnS$_2$ (curve-d) exhibits an increase. This increase can be attributed to the facile separation and transport of e$^-$/h$^+$ pairs facilitated by band alignment. After doping Cd into the composite (curve-e), the photocurrent response is further elevated. This suggests that the trap energy level introduced by Cd in the composite can promote photocurrent generation even further. However, the photocurrent decreased after Au loading (curve-f), indicating that Au competes for the absorption of incident light.

To further investigate the photocurrent generation mechanism, the valence band (VB SnO$_2$: + 3.91 eV, SnS$_2$: + 1.98 eV) and conduction band (CB SnO$_2$: + 0.24 eV, SnS$_2$: −0.11 eV) were obtained from band gap and flat band potential calculations. Figure S2 shows how the CB and VB were calculated from the photon energy and Mott-Schottky diagram. The introduction of trap energy levels through Cd^{3+} doping impedes the recombination and electron transfer of photo-generated e$^-$/h$^+$ pairs, thereby further amplifying the efficiency of photoelectric conversion and culminating in

the peak PEC response [34]. In addition, the photo-generated holes can be effectively quenched within the electrolyte environment featuring AA as an electron donor. This ultimately enhances the photoelectric current response. Figure 4B depicts the process of photo-generated electron transfer in the presence of AA within the electrolytic milieu of the sensor.

PEC and EIS characterization of PEC aptasensor preparation process

The stepwise construction process of the PEC aptasensor was documented through PEC measurements. As depicted in Fig. 4C, Au@Cd:SnO$_2$/SnS$_2$/CPE (curve-a) has the highest photocurrent response. Subsequently, cDNA (curve-b), BSA (curve-c), and E2-Apt (curve-d) are gradually modified on the surface of Au@Cd:SnO$_2$/SnS$_2$/CPE, and the intensity of the photocurrent is gradually weakened. This is because the aptamer hinders the

Fig. 4 **A** Photocurrent of CPE (a) pure carbon paste, (b) SnO_2, (c) SnS_2, (d) SnO_2/SnS_2, (e) $Cd:SnO_2/SnS_2$, (f) Au@$Cd:SnO_2/SnS_2$; **B** the electron transfer mechanism for Au@$Cd:SnO_2/SnS_2$; **C** Photocurrent response and **D** electrochemical impedance spectra (a) Au@$Cd:SnO_2/SnS_2$/CPE, (b) cDNA/Au@$Cd:SnO_2/SnS_2$/CPE, (c) BSA/cDNA/Au@$Cd:SnO_2/SnS_2$/CPE, (d) E2-Apt/BSA/cDNA/Au@$Cd:SnO_2/SnS_2$/CPE, (e) E2/E2-Apt/BSA/cDNA/Au@$Cd:SnO_2/SnS_2$/CPE
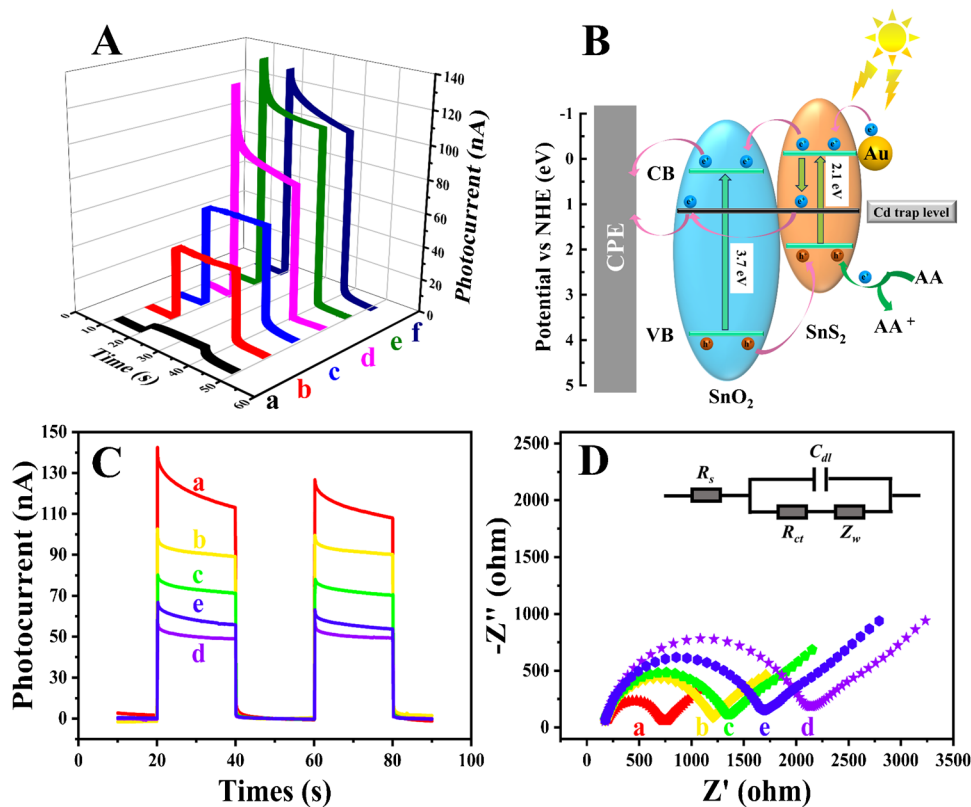
electron transfer and makes the reaction between the electron donor and the photo-generated hole less efficient. Curve-e demonstrates the photoelectric current response of the sensor after incubation with E2 (0.1 nmol L^{-1}). The formation of a complex between E2 and E2-Apt allows its dissociation from the electrode surface, reducing spatial hindrance and increasing the photoelectric current response.

Concurrently, the modified electrode underwent further characterization by utilizing electrochemical impedance spectroscopy (EIS). Illustrated in Fig. 4D, the Nyquist plot of Au@$Cd:SnO_2/SnS_2$/CPE (curve-a) demonstrates the smallest semicircular diameter (The charge transfer resistance (R_{ct}) value, being calculated from the diameter of the semicircle). Layer-by-layer modifications of cDNA (curve-b), BSA (curve-c), and E2-Apt (curve-d) onto the prepared Au@$Cd:SnO_2/SnS_2$/CPE gradually increase the R_{ct} value. Upon incubation with the tested substance E2 (curve-e), the R_{ct} value decreases. The inset figure in Fig. 4D represents the Randles equivalent circuit, and the fitting values are displayed in Table S2 using ZView software. Thus, the results obtained from EIS align with those obtained from the PEC current, further substantiating the successful construction of the PEC aptasensor.

Optimization of experimental conditions

To achieve the optimal photocurrent for E2 determination, key experimental factors related to the sensor, including the graphite-to-material ratio, concentration of AA, the effect of buffer pH values, and E2 incubation time, were meticulously optimized.

The proportion of graphite to the material during CPE preparation was carefully investigated (Fig. 5A). Excessive photoelectric material hinders the conductivity of the carbon paste, thus impeding the efficient transfer of photo-generated electrons to the electrode, resulting in reduced photocurrent. Conversely, an insufficient photoelectric material fails to provide a satisfactory photocurrent. Therefore, maintaining a 5:1 ratio between graphite and material yields the maximum photocurrent.

Figure 5B showed the influence of different AA concentrations on the photocurrent detected by the sensor. As the AA concentration increases from 0 to 0.8 mol L^{-1}, the photocurrent increases continuously and stabilizes above 0.8 mol L^{-1}. Hence, AA concentration of 1.0 mol L^{-1} was chosen as the optimal concentration for subsequent testing.

The influence of pH on the detection process was examined by studying various pH values of PBS. As illustrated in Fig. 5C, the PEC aptasensor had the highest photocurrent

Fig. 5 Optimization of experimental conditions: **A** graphite to material ratio, **B** concentration of AA, **C** pH value, **D** E2 incubation time (the E2 concentration with 1.0 nmol L^{-1})
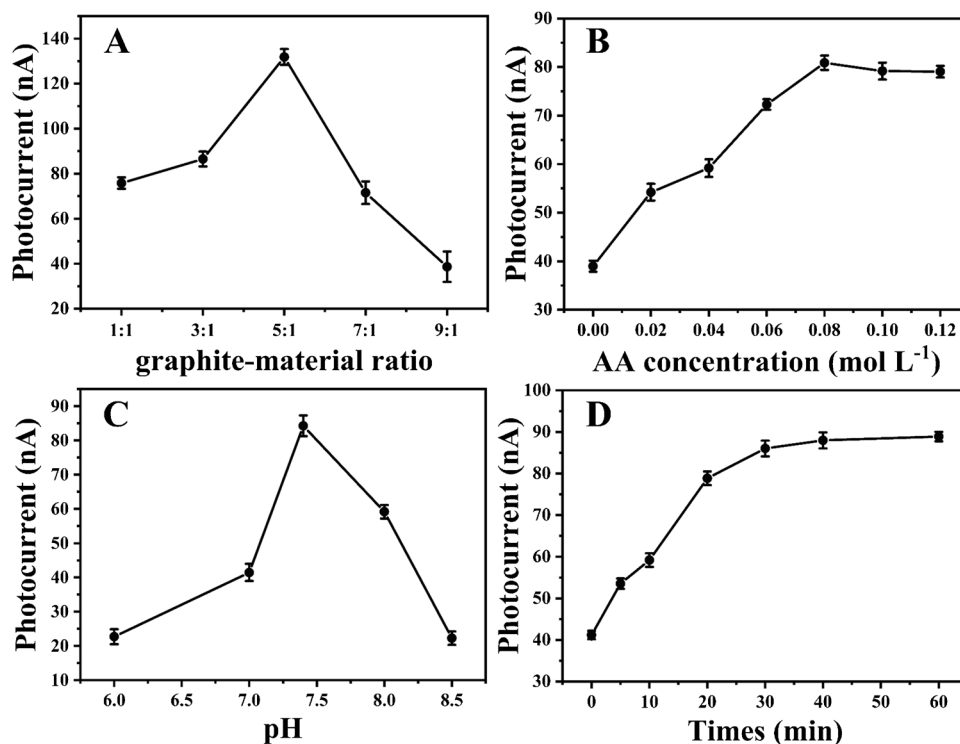
value at pH 7.4 among the different pH tests. It was ascribed to the reduction of the aptamer recognition activity in excessively acidic or alkaline environments, ultimately decaying the photocurrents [35]. Meanwhile, the detection environment of PBS solution with pH 7.4 was very close to physiological conditions. Therefore, pH 7.4 was selected as the most suitable for this experiment.

Finally, the variation of photocurrent with E2 incubation time was also investigated. As evidenced by Fig. 5D, a continuous increase in the photocurrent was observed as the incubation time progressed from 0 to 40 min. However, once the incubation time exceeds 40 min, the photocurrent tends to plateau, indicating the saturation of E2-Apt binding on the electrode surface. Therefore, an incubation time of 40 min was determined to be optimal for subsequent experiments.

The linearity of detecting E2

Under the above optimal conditions, we examined the performance of the PEC aptasensor for quantitative analysis of E2. The photocurrent is found to increase gradually with increasing estradiol concentrations (Fig. 6A). Figure 6B illustrates the linear relationship between PEC intensity ($\Delta I = I - I_0$, I_0 was defined as the photocurrent of the incubating blank) and the logarithm of E2 concentration (c, nmol L^{-1}) from 0.1 pmol L^{-1} to 3.2 nmol L^{-1}. The limit of detection was determined as 0.012 pmol L^{-1} (S/N = 3). The regression equation is expressed as ΔI (nA) = 4.12 log (c_{E2}, nmol L^{-1}) + 25.60 and the correlation coefficient of 0.992.

In comparison to several previously reported methods for detecting E2 (Table S3), the competitive-type PEC aptasensor demonstrates a wider linear range and lower detection limit.

Selectivity, stability, and reproducibility of the PEC aptasensor

To assess the specificity of the competitive-type PEC aptasensor, various interfering substances such as bovine serum albumin (BSA), bisphenol A (BPA), estriol (E3), testosterone (Testo), ethinylestradiol (EE), and glucose (Glu) were utilized. From Fig. 6C, even at 100 times the concentration of E2, the interference substances did not significantly change the sensor photocurrent response under the same testing conditions. However, when a mixture of interferents and E2 was present, there was a noticeable increase in photocurrent intensity, and this indicated that the PEC aptasensor had satisfactory selectivity and immunity to interference.

The experiments were conducted to measure the photocurrent stability. As observed in Fig. 6D, no significant variation was observed during the 15 cycles of on/off irradiation for 620 s while incubating with a concentration of 1.0 nmol L^{-1} E2, and the photocurrent value RSD was 2.62%. This confirms the outstanding stability of the photocurrent for detecting E2.

In addition, as illustrated in Fig. 6E, the PEC aptasensor was incubated with 1.0 nmol L^{-1} E2 and stored in a refrigerator at 4 °C for 14 days. Tests were conducted every few

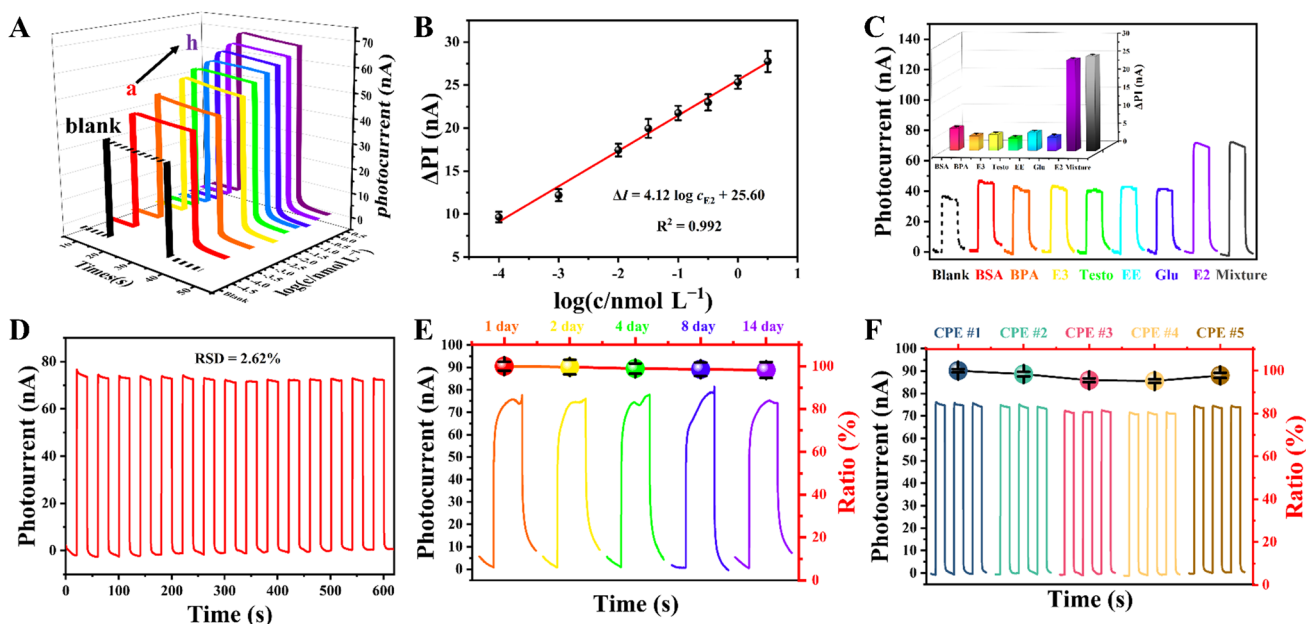**Fig. 6 A** Photocurrent response to variable concentration of E2: (a) 1×10^{-4} nmol L^{-1}, (b) 1×10^{-3} nmol L^{-1}, (c) 1×10^{-2} nmol L^{-1}, (d) 0.032 nmol L^{-1}, (e) 0.1 nmol L^{-1}, (f) 0.32 nmol L^{-1}, (g) 1 nmol L^{-1}, (h) 3.2 nmol L^{-1}; **B** the corresponding calibration curves; **C** photocurrent response of PEC aptasensor with blank, 100 nmol L^{-1} BSA, BPA, E3, Testo, EE, Glu, 1.0 nmol L^{-1} E2, and a mixture (contain-ing all the analytes); **D** photocurrent stability by 15 cycles of on/off irradiation for 620 s; **E** the photocurrent response of 1.0 nmol L^{-1} E2 by the same electrode stored in the refrigerator for 1~14 days and **F** photocurrent response of 1.0 nmol L^{-1} E2 detected by five sensors prepared under the same conditions. Error bars = SD ($n=3$)

days at room temperature, and the photocurrent decreased gradually. After 14 days, the photocurrent reached 95.2% of the initial test response, demonstrating excellent storage stability.

The reproducibility of the PEC aptasensor was evaluated by comparing the photocurrents of the five sensors prepared according to the method described in the "Regeneration of PEC aptasensor" section. All sensors were used with 1.0 nmol L^{-1} E2 as the target. The results are shown in Fig. 6F. The RSD was 2.59%, demonstrating that the PEC aptasensor has good reproducibility and that these sensing strategies are stable.

Detection of E2 in serum and river water samples by microfluidic device

To demonstrate the suitability for sample analysis, the PEC aptasensor was used to detect E2 in rat serum and river water samples. River water samples were taken from the school, and serum was collected from blood samples of the experimental rats. Firstly, different concentrations of E2 were added to the untreated rat serum samples (50 μL), and then the samples were pretreated with HClO$_4$ (5%, 50 μL) precipitation to remove interfering proteins. The supernatant was collected and diluted 100-fold with PBS buffer (pH 7.4) to minimize matrix effects. The spiked river water samples were filtered through a 0.45-μm membrane

and diluted with the same PBS. The slopes of the standard curves of E2 concentration established in rat serum and river water samples were similar to that in PBS (0.1 mol L^{-1}, pH = 7.4) (Fig. 7), so the E2 concentration in rat serum and river water was measured from the standard curves obtained in PBS solution. The concentration of E2 in the rat serum sample was measured to be 0.331 nmol L^{-1} (averaged from three measurements), and the simi-lar result was obtained to be 0.323 nmol L^{-1} (averaged from three measurements) using the liquid chromatog-raphy–mass spectrometry (LC-MS) [36]; the details was described in the "Actual sample detection" section of the Supplementary Information. The t-test analysis revealed that the P-value was larger than 0.05. This suggests that there is no statistically significant difference between the two methods. Furthermore, E2 was not detected in the river water sample, likely due to the concentration of E2 in the river water being below the detection limit. The con-centration of E2 in the measured samples was labeled as "Detected" in Table S4.

Recovery experiments were conducted using the standard addition method to demonstrate the accuracy of the results. Sample results were calculated by multiplying the test results of diluted samples by the dilution ratio. Determine the concentration of E2 in the mixed solution and label it as "Found" in Table S4. The recovery was analyzed according to the following formula.
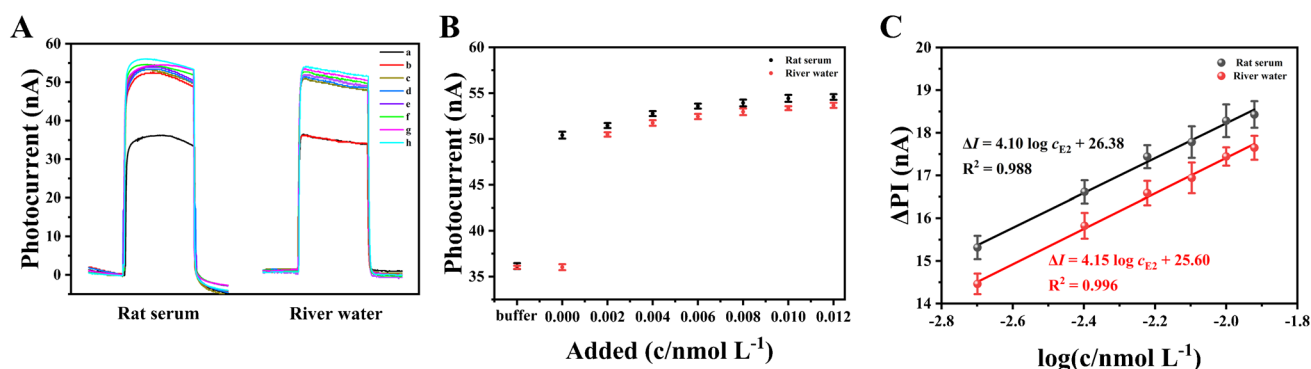
Fig. 7 A Photocurrent responses of spiked E2 in rat serum and river water. (a) Background signal in buffer, (b) actual sample without the addition of standard solution. The concentration of spiked E2 were (c) 0.2 nmol L^{-1}, (d) 0.4 nmol L^{-1}, (e) 0.6 nmol L^{-1}, (f) 0.8 nmol L^{-1}, (g) 1.0 nmol L^{-1}, and (h) 1.2 nmol L^{-1}. **B** Photocurrent signal in actual sample detection. **C** The corresponding calibration curves

$$Recovery(\%) = \frac{Found - Detected}{Added} \times 100\%$$

As shows in Table S4, the recovery rates ranged from 97.9 to 103.5%, with a relative standard deviation (RSD) of 2.10–4.71%. The repeatability and reproducibility of the sensors were also evaluated for the analysis of complex samples, as described in section "Repeatability and reproducibility" of the Supporting Information. The results demonstrated RSDs of 2.07% and 2.79% (Fig. S3) The above test results indicate that the developed PEC aptasensor exhibits a certain level of feasibility and potential practical value in the actual detection of E2.

Conclusion

In conclusion, a label-free competition strategy was used to develop a PEC aptasensor for the sensitive detection of estradiol. The sensor utilized a photoelectric sensing platform consisting of CPE loaded with Au@Cd:SnO$_2$/SnS$_2$, which allowed for stable photocurrent signals. This approach is found to be convenient, cost-effective, and efficient. To ensure good sensitivity and high selectivity for potential interference substances, the sensor employs a competitive structure formed by two complementary aptamers as the recognition unit. The microfluidic device allows for the rapid completion of POCT with fewer sampling. The practicality of this competitive PEC aptasensor was demonstrated through its application in rat serum and river water sample measurement, highlighting its broad potential for detecting endogenous substances.

Supplementary Information The online version contains supplementary material available at https://doi.org/10.1007/s00604-024-06478-y.

Author contribution Yonglun Zhang: conceptualization, methodology, writing—original draft, writing—review and editing. Shihua Zhang: formal analysis, investigation, validation. Zijing Xu: formal analysis, investigation. Jiaxing Zhang: writing—review and editing. Zhuang-zhuang Qu: resources. Weilu Liu: conceptualization, writing—review and editing, project administration, supervision

Data availability All data generated or analysed during this study are included in this published article [and its supplementary information files].

Declarations

Ethical approval Animal experiments were conducted according to the guidelines formulated by the Ethics Committee of Shenyang Pharmaceutical University (SYPU-IACUC-2024-0311-028).

Conflict of interest The authors declare no competing interests.

References

1. Fuentes N, Nicoleau M, Cabello N, Montes D, Zomorodi N, Chroneos ZC, Silveyra P (2019) 17beta-Estradiol affects lung function and inflammation following ozone exposure in a sex-specific manner. Am J Physiol Lung Cell Mol Physiol 317(5):L702–L716. https://doi.org/10.1152/ajplung.00176.2019
2. Nezami A, Nosrati R, Golichenari B, Rezaee R, Chatzidakis GI, Tsatsakis AM, Karimi G (2017) Nanomaterial-based aptasensors and bioaffinity sensors for quantitative detection of 17β-estradiol. TrAC Trends Anal Chem 94:95–105. https://doi.org/10.1016/j.trac.2017.07.003

3. Pezzolato M, Maurella C, Varello K, Meloni D, Bellino C, Borlatto L, Di Corcia D, Capra P, Caramelli M, Bozzetta E (2011) High sensitivity of a histological method in the detection of low-dosage illicit treatment with 17β-estradiol in male calves. Food Control 22(10):1668–1673. https://doi.org/10.1016/j.foodcont.2011.03.027

4. Russell N, Grossmann M (2019) Mechanisms in endocrinology: Estradiol as a male hormone. Eur J Endocrinol 181(1):R23–R43. https://doi.org/10.1530/eje-18-1000

5. Godfray HCJ, Stephens AEA, Jepson PD, Jobling S, Johnson AC, Matthiessen P, Sumpter JP, Tyler CR, McLean AR (2019) A restatement of the natural science evidence base on the effects of endocrine disrupting chemicals on wildlife. Proc Biol Sci 286(1897):2416–2427. https://doi.org/10.1098/rspb.2018.2416

6. Gaikwad NW (2013) Ultra performance liquid chromatography-tandem mass spectrometry method for profiling of steroid metabolome in human tissue. Anal Chem 85(10):4951–4960. https://doi.org/10.1021/ac400016e

7. Azzouz A, Ballesteros E (2015) Multiresidue method for the determination of pharmacologically active substances in egg and honey using a continuous solid-phase extraction system and gas chromatography-mass spectrometry. Food Chem 178:63–69. https://doi.org/10.1016/j.foodchem.2015.01.044

8. Arabi M, Ostovan A, Li J, Wang X, Zhang Z, Choo J, Chen L (2021) Molecular imprinting: green perspectives and strategies. Adv Mater 33(30):e2100543. https://doi.org/10.1002/adma.202100543

9. Arabi M, Chen L (2022) Technical challenges of Molecular-Imprinting-based optical sensors for environmental pollutants. Langmuir 38(19):5963–5967. https://doi.org/10.1021/acs.langmuir.2c00935

10. Arabi M, Ostovan A, Wang Y, Mei R, Fu L, Li J, Wang X, Chen L (2022) Chiral molecular imprinting-based SERS detection strategy for absolute enantiomeric discrimination. Nat Commun 13(1):5757. https://doi.org/10.1038/s41467-022-33448-w

11. Ge L, Liu Q, Hao N, Kun W (2019) Recent developments of photoelectrochemical biosensors for food analysis. J Mater Chem B 7(46):7283–7300. https://doi.org/10.1039/c9tb01644a

12. Aydin EB, Sezginturk MK (2017) Indium tin oxide (ITO): a promising material in biosensing technology. TrAC Trends Anal Chem 97:309–315. https://doi.org/10.1016/j.trac.2017.09.021

13. Hu Y, Wang K, Zhang Q, Li F, Wu T, Niu L (2012) Decorated graphene sheets for label-free DNA impedance biosensing. Biomaterials 33(4):1097–1106. https://doi.org/10.1016/j.biomaterials.2011.10.045

14. Yazhini K, Suja SK, Kalaivani GJ, Bagyalaksmi J, Pavalamalar S (2018) Non-enzymatic sensing of kidney dysfunction biomarker using pectin - MWCNT nanocomposite. Appl Surf Sci 449:736–744. https://doi.org/10.1016/j.apsusc.2018.01.197

15. Alves GM, da Silva JL, Stradiotto NR (2021) A novel citrus pectin-modified carbon paste electrochemical sensor used for copper determination in biofuel. Measurement 169:380–390. https://doi.org/10.1016/j.measurement.2020.108356

16. Zhu J-H, Gou H, Zhao T, Mei L-P, Wang A-J, Feng J-J (2022) Ultrasensitive photoelectrochemical aptasensor for detecting telomerase activity based on Ag2S/Ag decorated ZnIn2S4/C3N4 3D/2D Z-scheme heterostructures and amplified by Au/Cu2+-boron-nitride nanozyme. Biosens Bioelectron 203. https://doi.org/10.1016/j.bios.2022.114048

17. Cheng F, Liang J, Tao Z, Chen J (2011) Functional materials for rechargeable batteries. Adv Mater 23(15):1695–1715. https://doi.org/10.1002/adma.201003587

18. Hu L, Chen F, Hu P, Zou L, Hu X (2016) Hydrothermal synthesis of SnO2/ZnS nanocomposite as a photocatalyst for degradation of rhodamine B under simulated and natural sunlight. J Mol Catal A: Chem 411:203–213. https://doi.org/10.1016/j.molcata.2015.10.003

19. Zhang Z, Wang L, Xiao J, Xiao F, Wang S (2015) One-pot synthesis of three-dimensional graphene/carbon nanotube/SnO2 hybrid architectures with enhanced lithium storage properties. ACS Appl Mater Interfaces 7(32):17963–17968. https://doi.org/10.1021/acsami.5b04673

20. Deng L, Zhu Z, Liu L, Liu H (2017) Synthesis of Ag2O and Ag co-modified flower-like SnS2 composites with enhanced photocatalytic activity under solar light irradiation. Solid State Sci 63:76–83. https://doi.org/10.1016/j.solidstatesciences.2016.11.016

21. Zhang YC, Yao L, Zhang G, Dionysiou DD, Li J, Du X (2014) One-step hydrothermal synthesis of high-performance visible-light-driven SnS2/SnO2 nanoheterojunction photocatalyst for the reduction of aqueous cr(VI). Appl Catal B 144:730–738. https://doi.org/10.1016/j.apcatb.2013.08.006

22. Fan C, Plaxco KW, Heeger AJ (2003) Electrochemical interrogation of conformational changes as a reagentless method for the sequence-specific detection of DNA. 100(16):9134–9137. https://doi.org/10.1073/pnas.1633515100

23. Herne TM, Tarlov MJ (1997) Characterization of DNA Probes immobilized on gold surfaces. J Am Chem Soc 119(38):8916–8920. https://doi.org/10.1021/ja9719586

24. Cox JC, Ellington AD (2001) Automated selection of anti-protein aptamers. Bioorg Med Chem 9(10):2525–2531. https://doi.org/10.1016/s0968-0896(01)00028-1

25. Kim YS, Jung HS, Matsuura T, Lee HY, Kawai T, Gu MB (2007) Electrochemical detection of 17 beta-estradiol using DNA aptamer immobilized gold electrode chip. Biosens Bioelectron 22(11):2525–2531. https://doi.org/10.1016/j.bios.2006.10.004

26. Eisold A, Labudde D (2018) Detailed analysis of 17beta-estradiol-aptamer interactions: a molecular dynamics simulation study. Molecules 23(7):747–769. https://doi.org/10.3390/molecules23071690

27. Alsager OA, Kumar S, Zhu B, Travas-Sejdic J, McNatty KP, Hodgkiss JM (2015) Ultrasensitive colorimetric detection of 17beta-estradiol: the effect of shortening DNA aptamer sequences. Anal Chem 87(8):4201–4209. https://doi.org/10.1021/acs.analchem.5b00335

28. Green MA, Ho-Baillie A, Snaith HJ (2014) The emergence of perovskite solar cells. Nat Photonics 8(7):506–514. https://doi.org/10.1038/nphoton.2014.134

29. Maestre D, Hernández E, Cremades A, Amati M, Piqueras J (2012) Synthesis and characterization of small dimensional structures of Er-Doped SnO2 and erbium–tin–oxide. Cryst Growth Des 12(5):2478–2484. https://doi.org/10.1021/cg300106k

30. Mo F, Wu J, Chen M, Meng H, Han Q, Fu Y (2019) Enzyme-free on-off-on photoelectrochemical biosensor based on cascaded quadratic amplification strategy for miRNA 141 detection. Sens Actuators B: Chem 289:269–276. https://doi.org/10.1016/j.snb.2019.03.044

31. Feng R, Tian K, Zhang Y, Liu W, Fang J, Khan MS, Wei Q, Wu R (2020) Recognition of M2 type tumor-associated macrophages with ultrasensitive and biocompatible photoelectrochemical cytosensor based on ce doped SnO(2)/SnS(2) nano heterostructure. Biosens Bioelectron 165:112367–112375. https://doi.org/10.1016/j.bios.2020.112367

32. Liu X, Liu P, Tang Y, Yang L, Li L, Qi Z, Li D, Wong DKY (2018) A photoelectrochemical aptasensor based on a 3D flower-like TiO2-MoS2-gold nanoparticle heterostructure for detection of kanamycin. Biosens Bioelectron 112:193–201. https://doi.org/10.1016/j.bios.2018.04.041

33. Li Z, Ng KH, Xu S, Zhang Y, Lei Y, Huang J, Lai Y (2022) Facile preparation of tremella-like TiO(2)/Cd:ZnIn(2)S(4) photoanode with enhanced photo-electro-chemical (PEC) performance for energy and environmental applications. Chemosphere 307:135758–135767. https://doi.org/10.1016/j.chemosphere.2022.135758

34. Huang H, Xiao K, Dong F, Wang J, Du X, Zhang Y (2016) Sulfur-doping synchronously ameliorating band energy structure and charge separation achieving decent visible-light photocatalysis of Bi2O2CO3. RSC Adv 6(97):94361–94364. https://doi.org/10.1039/c6ra04888a

35. Hasegawa H, Savory N, Abe K, Ikebukuro K (2016) Methods for improving aptamer binding Affinity. Molecules 21(4):421. https://doi.org/10.3390/molecules21040421

36. Liu W, Li H, Yu S, Zhang J, Zheng W, Niu L, Li G (2018) Poly(3,6-diamino-9-ethylcarbazole) based molecularly imprinted polymer sensor for ultra-sensitive and selective detection of 17-β-estradiol in biological fluids. Biosens Bioelectron 104:79–86. https://doi.org/10.1016/j.bios.2018.01.002